

## Highlights

### **Impacts of Hurricane Irma (2017) on ocean transport processes**

Thomas Dobbelaere, Milan Curcic, Matthieu Le Hénaff, Emmanuel Hanert

- The coupled SLIM+SWAN model correctly reproduces the hydrodynamics and waves during Irma.
- Wave radiation stress increases currents by up to 1 m/s during Irma.
- Wave radiation stress gradients are the largest on the shelf break and over reefs.
- Waves can deflect drifting particles by up to 20 km during the hurricane.
- The Stokes drift has a larger impact on transport than the wave radiation stress.

# Impacts of Hurricane Irma (2017) on ocean transport processes

Thomas Dobbelaere<sup>a,\*</sup>, Milan Curcic<sup>b</sup>, Matthieu Le Hénaff<sup>c,d</sup>, Emmanuel Hanert<sup>a,e</sup>

<sup>a</sup>*Eath and Life Institute (ELI), UCLouvain, Louvain-la-Neuve, Belgium*

<sup>b</sup>*Rosenstiel School of Marine and Atmospheric Sciences (RSMAS), University of Miami, Coral Gables, Florida, USA*

<sup>c</sup>*Cooperative Institute for Marine and Atmospheric Studies (CIMAS), University of Miami, Miami, Florida, USA*

<sup>d</sup>*Atlantic Oceanographic and Meteorological Laboratory (AOML), NOAA, Miami, Florida, USA*

<sup>e</sup>*Institute of Mechanics, Materials and Civil Engineering (IMMC), UCLouvain, Louvain-la-Neuve, Belgium*

---

## Abstract

Tropical cyclones are becoming more intense and more frequent. Their effect is particularly acute in coastal areas where they cause extensive damage leading to an influx of debris, sediments and waste to the sea. However, most coastal ocean models do not represent heavy-wind transport processes correctly as they do not couple the hydrodynamics with the wind-generated waves [Change this sentence]. This may lead to significant errors in ocean simulations under tropical cyclone conditions. Here, we investigate current-wave interactions during a major hurricane and assess their impact on transport processes. We do that by coupling the unstructured-mesh coastal ocean model SLIM with the spectral wave model SWAN, and applying it to the Florida Reef Tract during Hurricane Irma (September 17). We show that the coupled model successfully reproduces the wave behavior, the storm surge and the ocean currents during the passage of the hurricane. We then use the coupled and

---

\*Corresponding author

Email address: [thomas.dobbelaere@uclouvain.be](mailto:thomas.dobbelaere@uclouvain.be) (Thomas Dobbelaere)

uncoupled wave-current model to simulate the transport of passive drifters. We show that the wave radiation stress gradient alone can lead to changes of up to 1 m/s in the modeled currents, which in turn leads to differences of up to 5 km in the position of drifting material over the duration of the hurricane. The Stokes drift however appears to cause deflections up to 4 times more intense and should thus be considered in priority. Wave-current interactions therefore strongly impact the transport of drifting material such as sediments and debris in the aftermath of a hurricane. They should thus be taken into account in order to correctly assess its overall impact.

*Keywords:* Hurricane, Ocean transport, Wave-current interactions

---

## **1. Introduction**

2 Tropical cyclones are becoming more intense and more frequent (Bhatia  
3 et al., 2019; Kossin et al., 2020). This increase is likely due to climate  
4 change and will probably continue in the future (Knutson et al., 2020).  
5 However, estimating the impact of tropical cyclones on the coastal ocean  
6 circulation remains a challenge. Understanding wave-current interactions  
7 and representing their impact on coastal ocean transport processes is central  
8 to many coastal activities such as dredging, erosion management, oil and  
9 gas activities, search and rescue, and insurance (Bever and MacWilliams,  
10 2013; Li and Johns, 1998; Breivik et al., 2013). All these activities require  
11 wave-current models to predict the impact of tropical cyclones on the coastal  
12 circulation and on water-level changes.

13 Wave-current interactions during a cyclone are highly nonlinear and vary  
14 significantly in space and time (Wu et al., 2011). Wave-induced currents  
15 are generated by wave radiation stress gradients (Longuet-Higgins, 1970),  
16 affecting water levels near shorelines and wave breaking points (Longuet-  
17 Higgins and Stewart, 1964). Changes in water levels and currents, in turn,  
18 affect the motion and evolution of the waves (Sikirić et al., 2013). Coupled  
19 wave-current models hence require the calculation of the full directional

20 wave spectrum in order to correctly reproduce the dynamics of wind-driven  
21 surface waves. This is usually achieved by spectral wave models, which  
22 describe the evolution of the wave energy spectrum. As of today, the most  
23 popular spectral wave models are WAM (WAMDI Group, 1988), SWAN (Booij  
24 et al., 1999), and WAVEWATCH III (Tolman et al., 2009). Among these  
25 models, SWAN has been specifically developed for coastal applications, as  
26 it represents depth-induced wave breaking and triad wave-wave interactions  
27 using numerical techniques adapted to small-scale, shallow water regions  
28 (Booij et al., 1999). However, WAVEWATCH III has recently been equipped  
29 with new parallelization algorithm, domain decomposition and numerical  
30 schemes for high resolution coastal applications (WW3DG, 2019; Abdolali  
31 et al., 2020).

32 [Paragraph about wave-currents interaction during TCs to cite papers  
33 from reviewer 4]

34 Coastal oceans are characterized by the complex topography of the coast-  
35 line and the presence of islands, reefs and artificial structures. Traditional  
36 structured-grid models lack the flexibility to simulate near-shore processes at  
37 a sufficiently small scale. Although the use of nested structured grids allows  
38 to locally refine the model resolution (Warner et al., 2010), staircase-like  
39 representation of complex coastal topographies cannot be avoided. Instead,  
40 unstructured-mesh models easily adapt to the topography and are hence  
41 better suited to coastal processes (Fringer et al., 2019). Capturing the impact  
42 of the topography on wave interactions becomes even more important in  
43 the case of tropical cyclones. Heavy winds generate large wind-waves and  
44 disturb ocean conditions (Liu et al., 2020) by causing coastal upwellings on  
45 continental shelves (Smith, 1982) and inducing strong currents, waves and  
46 storm surges in nearshore and coastal regions (Dietrich et al., 2010; Weisberg  
47 and Zheng, 2006).

48 Heavy wind conditions also affect material transport at the ocean surface.  
49 The transport of drifting objects or substances that are locally released is often

best represented by a Lagrangian individual-based model. Such an approach is routinely used to model the dispersal of larvae, pollutants, sediments and many other tracers (e.g. Le Hénaff et al., 2012; Liubartseva et al., 2018; Figueiredo et al., 2013; Frys et al., 2020). Although some transport models take the impact of waves into account by adding a Stokes drift velocity, *i.e.* the net drift of a floating particle in the direction of the wave propagation (Van Den Bremer and Breivik, 2018), to the Eulerian currents, they usually neglect the wave-induced currents. Such practice is reasonable in fair weather, when wave-induced forces exerted on currents are relatively small, but may lead to significant errors during storm conditions (Röhrs et al., 2012; Curcic et al., 2016).

The objective of this study is therefore to assess the importance of wave-current interactions during a tropical cyclone. We investigate the transport of drifting particles on the Florida shelf during Hurricane Irma, one of the strongest and costliest tropical cyclones on record in the Atlantic Basin (Xian et al., 2018), which made landfall in Florida in September 2017. To do that, we developed an unstructured-mesh coupled wave-current model of South Florida to simulate the ocean circulation under hurricane conditions. Both modeled currents and waves were validated against field measurements and then used to simulate the transport of drifting material in the Florida Keys and the Florida inner shelf. Model outputs were then compared with uncoupled simulation results in order to assess the impact of wave-induced forces and Stokes drift on the modeled currents and transports.

## 2. Methods

### 2.1. Study area and observational data

This study focuses on the South of Florida, as highlighted in Fig. 1. The large-scale ocean circulation around South Florida is dominated by the Florida Current (FC), which originates from the Loop Current (LC) where it enters the Florida Straits from the Gulf of Mexico, and, downstream, forms

79 the Gulf Stream. The FC is a major western boundary current characterized  
80 by spatial variability and meandering, associated with the presence of cyclonic  
81 eddies between the core of the current and the complex reef topography  
82 of the Florida Reef Tract (FRT) (Lee et al., 1995; Kourafalou and Kang,  
83 2012). The variability of the FC extends over a large range of spatial and  
84 temporal scales, with periods of 30-70 days in the Lower Keys (Lee et al., 1995)  
85 and shorter periods of 2-21 days in the Upper Keys (Lee and Mayer, 1977),  
86 and exhibits significant seasonal and interannual cycles (Johns and Schott,  
87 1987; Lee and Williams, 1988; Schott et al., 1988). Circulation on the West  
88 Florida Shelf (WFS), on the other hand, is forced by local winds and tidal  
89 fluctuations (Lee and Smith, 2002; Liu and Weisberg, 2012). Furthermore,  
90 due to its location relative to the warm waters of the North Atlantic, Florida  
91 is particularly vulnerable to tropical cyclones. On average, the state gets  
92 hit by a hurricane every two years and strong hurricanes, some of which are  
93 among the most destructive on record, strike Florida on average once every  
94 four years (Malmstadt et al., 2009).

95 The state of the ocean around Florida is monitored by an extensive  
96 array of tide gauges, current meters and buoys. In this study, we used sea  
97 surface elevation measurements from the National Oceanic and Atmospheric  
98 Administrations (NOAA) Tides and Currents dataset. These measurements  
99 were taken at four locations: two in the Florida Keys (Key West and Vaca  
100 Key); one on the East coast of Florida (Virginia Key); and one on the West  
101 coast (Naples). For the currents, we used ADCP measurements from the  
102 University of South Florida's College of Marine Science's (USF/CMS) Coastal  
103 Ocean Monitoring and Prediction System (COMPS) for the WFS (Weisberg  
104 et al., 2009). More specifically, we used measurements from moorings C10,  
105 C12 and C13, respectively located at the 25, 50, and 50 m isobaths of the  
106 WFS (Liu et al., 2020). Finally, for the waves, we used measurements from  
107 four buoys of the NOAA's National Data Buoy Center (NDBC); two on  
108 Florida's eastern shelf and two on the WFS. The locations of all measurement

109 stations are shown in Fig. 1.

110 *2.2. Wind and atmospheric pressure during Hurricane Irma*

111 Hurricane Irma made landfall in Florida on 10 September 2017 as a  
112 category 4 hurricane at Cudjoe Key (Florida Keys) and later as a category  
113 3 hurricane on Marco Island, south of Naples (see hurricane track in Fig.  
114 1). It then weakened to a category 2 hurricane as it moved further inland  
115 (Cangialosi et al., 2018). The storm damaged up to 75% of the buildings  
116 at its landfall point in the Florida Keys, making it one of the strongest and  
117 costliest hurricanes on record in the Atlantic basin (Xian et al., 2018; Zhang  
118 et al., 2019). The strongest reported sustained winds on Marco Island was  
119 50 m/s while the highest recorded storm surge was 2.3 m, although larger  
120 wind speed likely occurred in the Florida Keys (Pinelli et al., 2018). To  
121 reproduce the wind profile of Irma in our model, we used high-resolution  
122 H\*Wind wind fields (Powell et al., 1998). As these data represent 1-min  
123 averaged wind speeds, we multiplied them by a factor 0.93 to obtain 10-min  
124 averaged wind speeds (Harper et al., 2010). This conversion factor accounts  
125 for the greater variance of mean winds measured over periods shorter than  
126 10 minutes, therefore producing more erratic value. Furthermore, H\*Wind  
127 wind profiles did not cover the whole model extent during the passage of the  
128 hurricane and were thus blended within coarser wind field extracted from  
129 ECMWF ERA-5 datasets (Fig. 2A). The pressure field during the passage  
130 of Hurricane Irma was also reconstructed using ERA-5 data. However, the  
131 coarse resolution of the dataset smoothes out the depression at the center of  
132 the hurricane, leading to an underestimation of the pressure gradient (Fig.  
133 2B). To better capture the central depression of Irma, we therefore built a  
134 hybrid pressure field using the position and the minimal pressure of the core  
135 of the hurricane based on its track as recorded in the HURDAT 2 database  
136 (Landsea and Franklin, 2013). Based on this information, the hybrid pressure  
137 field was constructed by combining an idealized Holland pressure profile (Lin  
138 and Chavas, 2012) within the radius of maximum wind speed of Irma (Knaff

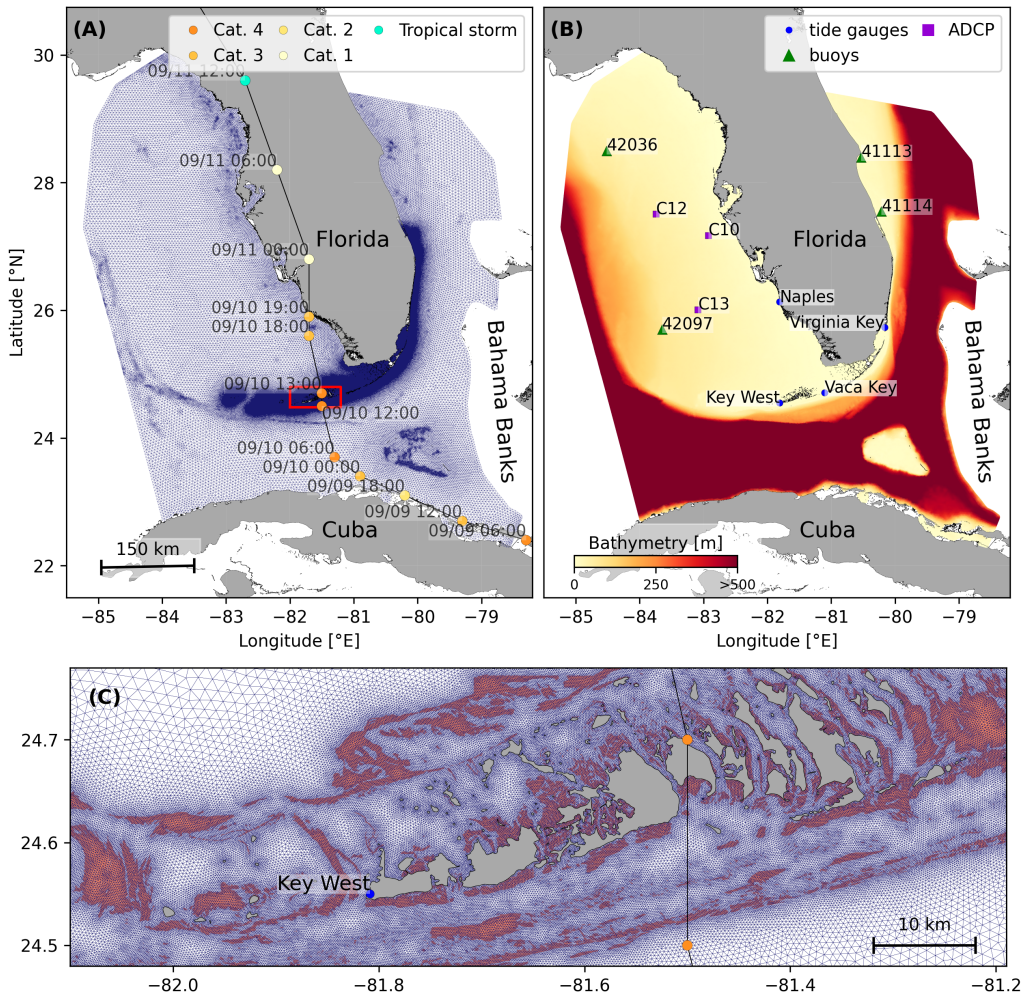


**Fig. 1:** (A) Mesh of the computational domain with the trajectory of Irma. The category of the hurricane is given by the Saffir-Simpson color scale. (B) Bathymetry of the domain with the location of stations used for the validation of the model outputs. (C) Close up view of the Lower Keys area (red squares in (A)), where the mesh resolution reaches 100 m near reefs (shown in dark orange) and islands (highlighted in dark grey)

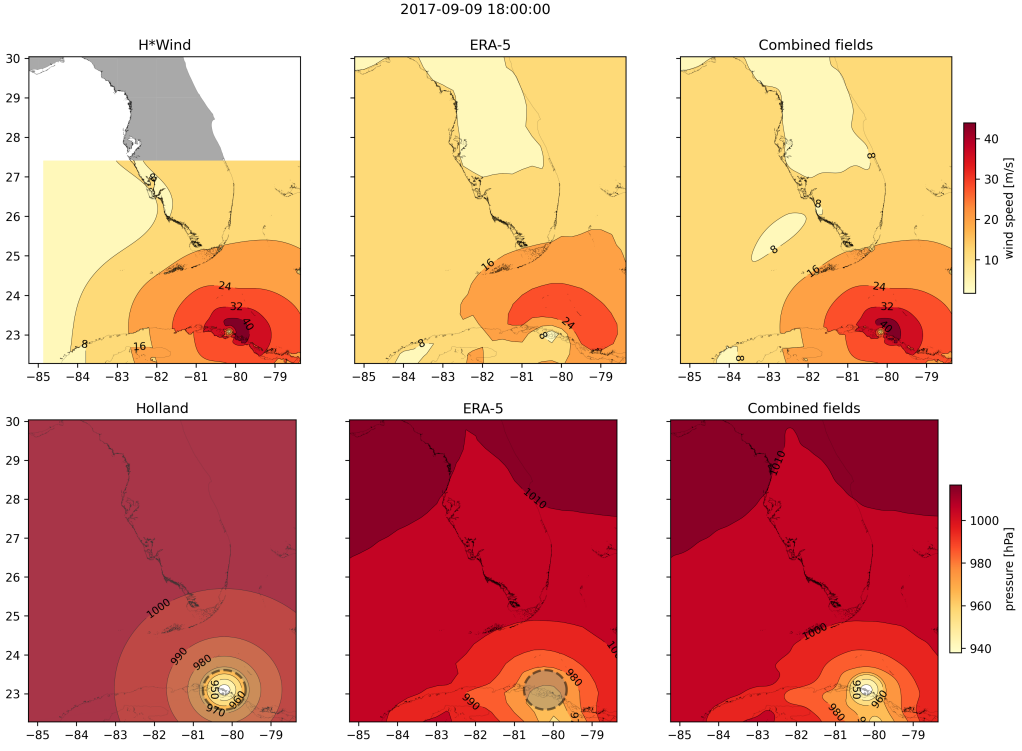


**Fig. 2:** Snapshot of the hybrid wind (top) and pressure (bottom) profiles constructed to capture the passage of Hurricane Irma at 1800 UTC on 9 September 2017. Wind profiles are obtained by combining high resolution H\*Wind with coarser ERA-5 wind fields. The pressure field is built by combining the ERA-5 pressure field with an idealized Holland pressure profile based on the track of Irma in the HURDAT 2 database. Holland field was only used within the radius of maximum wind speed (dashed grey line) of the hurricane to capture its central depression.

139 et al., 2018) with ERA-5 pressure field. The transition from the Holland  
 140 profile to ERA-5 data outside the radius of maximum wind speed data was  
 141 performed using a smooth step function (Fig. 2).

142 *2.3. Hydrodynamic model*

143 Ocean currents generated during hurricane Irma around South Florida  
 144 were modeled using the 2D barotropic version of the unstructured-mesh

145 coastal ocean model SLIM<sup>1</sup> (Lambrechts et al., 2008). The model mesh covers  
 146 an area similar to the model extent of Dobbelaere et al. (2020), that includes  
 147 the FRT but also the Florida Straits and part of the Gulf of Mexico (Figure 1).  
 148 However, this area has been slightly extended northeastward and westward  
 149 in order to include the NOAA-NDBC buoys. Furthermore, to withstand  
 150 potential cell drying during the hurricane, we solved the conservative shallow  
 151 water equations with wetting-drying:

$$\begin{aligned}
 \frac{\partial H}{\partial t} + \nabla \cdot (\mathbf{U}) &= 0 , \\
 \frac{\partial \mathbf{U}}{\partial t} + \nabla \cdot \left( \frac{\mathbf{U}\mathbf{U}}{H} \right) + f\mathbf{e}_z \times \mathbf{U} &= \alpha g H \nabla(H - h) - \frac{1}{\rho} \nabla p_{\text{atm}} + \frac{1}{\rho} \boldsymbol{\tau}_s \\
 &\quad + \nabla \cdot (\nu \nabla \mathbf{U}) - \frac{C_b}{H^2} |\mathbf{U}| \mathbf{U} + \gamma (\mathbf{U}_{\text{ref}} - \mathbf{U}) ,
 \end{aligned} \tag{1}$$

152 where  $H$  is the water column height and  $\mathbf{U}$  is the depth-averaged transport;  
 153  $f$  is the Coriolis coefficient;  $g$  is the gravitational acceleration;  $h$  is the  
 154 bathymetry;  $\alpha$  is a coefficient indicating whether the mesh element is wet  
 155 ( $\alpha = 1$ ) or dry ( $\alpha = 0$ ) (Le et al., 2020);  $\nu$  is the viscosity;  $C_b$  is the bulk  
 156 bottom drag coefficient;  $p_{\text{atm}}$  is the atmospheric pressure;  $\boldsymbol{\tau}_s$  is the surface  
 157 stress, usually due to wind; and  $\gamma$  is a relaxation coefficient towards a reference  
 158 transport  $\mathbf{U}_{\text{ref}}$ . As this study focuses on transport processes and not coastal  
 159 flooding, wetting-drying is only applied on wet grid cells that may become dry  
 160 under the influence of the hurricane. As in Frys et al. (2020) and Dobbelaere  
 161 et al. (2020), SLIM currents were gradually relaxed towards the operational  
 162 Navy HYCOM product (GOMl0.04<sup>2</sup>, Chassignet et al. (2007)) in regions where  
 163 the water depth exceeds 50 m. HYCOM's 3D currents were depth-integrated  
 164 into 2D transports to be used as forcing in the model. Moreover, these

---

<sup>1</sup><https://www.slim-ocean.be>

<sup>2</sup><https://www.hycom.org/data/goml0pt04>

165 transports as well as HYCOM's sea surface elevation were used as boundary  
166 condition in the model.

167 We adapted the parameterization of the wind-induced surface stress to  
168 storm conditions. At very high wind speeds, the white cap is blown off  
169 the crest of the waves. This phenomenon, also known as spume, has been  
170 hypothesized to generate a layer of droplets that acts as a slip layer for the  
171 winds at the ocean-atmosphere interface (Holthuijsen et al., 2012). It causes  
172 a saturation of the wind drag coefficient for strong winds (Powell et al., 2003;  
173 Donelan et al., 2004; Curcic and Haus, 2020). We take this saturation effect  
174 into account by using the wind drag parameterization of Moon et al. (2007).  
175 In this parameterization, the drag coefficient  $C_d$  depends on the wind speed  
176 at 10-m height  $U_{10}$  according to:

$$C_d = \kappa^2 \log \left( \frac{10}{z_0} \right)^{-2} \quad (2)$$

177 where  $\kappa$  is the von Karman constant and  $z_0$  is the roughness length expressed  
178 as:

$$z_0 = \begin{cases} \frac{0.0185}{g} u_*^2 & \text{if } U_{10} \leq 12.5 \text{ m/s ,} \\ [0.085(-0.56u_*^2 + 20.255u_*) + 2.458] \times 10^{-3} & \text{if } U_{10} > 12.5 \text{ m/s ,} \end{cases} \quad (3)$$

179 with  $u_*$  the friction velocity. The relation between  $U_{10}$  and  $u_*$  is given by:

$$U_{10} = -0.56u_*^2 + 20.255u_* + 2.458 . \quad (4)$$

180 The mesh resolution depends on the distance to the coastlines and reefs  
181 following the approach of Dobbelaere et al. (2020). The mesh is then further  
182 refined according to bathymetry value and gradient, as suggested in the  
183 SWAN user-guide<sup>3</sup>. Such an approach improves the model efficiency as the

---

<sup>3</sup><http://swanmodel.sourceforge.net/unswan/unswan.htm>

184 mesh resolution is only increased where required by the currents and waves  
 185 dynamics. The mesh was generated with the seamsh<sup>4</sup> Python library, which is  
 186 based on the the open-source mesh generator GMSH (Geuzaine and Remacle,  
 187 2009). It is composed of approximately  $7.7 \times 10^5$  elements. The coarsest  
 188 elements, far away from the FRT, have a characteristic length of about 5 km  
 189 whereas the finest elements have a characteristic length of about 100 m along  
 190 the coastlines and over the reefs (Fig 1).

191 *2.4. Wave model*

192 Waves were modeled using the parallel unstructured-mesh version of the  
 193 Simulating WAves Nearshore (SWAN) model (Booij et al., 1999), one of the  
 194 most popular wave models for coastal areas and inland waters. It solves the  
 195 action balance equation (Mei, 1989):

$$\frac{\partial N}{\partial t} + \nabla_{\mathbf{x}} \cdot [(\mathbf{c}_g + \mathbf{u})N] + \frac{\partial}{\partial \theta}[c_\theta N] + \frac{\partial}{\partial \sigma}[c_\sigma N] = \frac{S_{in} + S_{ds} + S_{nl}}{\sigma}, \quad (5)$$

196 where  $N = E/\sigma$  is the wave action density and  $E$  is the wave energy spectrum;  
 197  $\theta$  is the wave propagation direction;  $\sigma$  is the intrinsic wave frequency;  $\mathbf{c}_g$  is  
 198 the wave group velocity,  $\mathbf{u} = \mathbf{U}/H$  is SLIM depth-averaged current velocity;  
 199  $c_\theta$  and  $c_\sigma$  are the propagation velocities in spectral space due to refraction  
 200 and shifting in frequency due to variations in depth and currents; and  $S_{in}$ ,  
 201  $S_{ds}$ , and  $S_{nl}$  respectively represent wave growth by wind, wave decay and  
 202 nonlinear transfers of wave energy through four and three-wave interactions,  
 203 *i.e.* quadruplets and triplets. The wave spectra were discretized with 48  
 204 direction bins and 50 frequency bins logarithmically distributed from 0.03 to  
 205 2 Hz. Exponential wind growth was parameterized using the formulation of  
 206 Janssen (1991), while dissipations by whitecapping and bottom dissipation  
 207 followed the formulations of Komen et al. (1984) and Madsen et al. (1989),  
 208 respectively.

---

<sup>4</sup><https://pypi.org/project/seamsh/>

209 Coefficients for exponential wind growth and whitecapping parameteriza-  
 210 tions were based on the results of Siadatmousavi et al. (2011), and significantly  
 211 differ from SWAN’s default settings. By default, SWAN implements the wind  
 212 input formulation of Komen et al. (1984) and the steepness-dependent co-  
 213 efficient governing dissipation by whitecapping is a linear function of the  
 214 wavenumber. In this study, this steepness-dependent coefficient is a quadratic  
 215 function of the wavenumber, as it showed better predictions of the significant  
 216 wave height in the study of Siadatmousavi et al. (2011). The choice of these  
 217 formulations was motivated by the appearance of numerical instabilities in  
 218 the region of the Gulf Stream when using SWAN’s default parameter values.  
 219 Finally, ERA5 wave spectra was used as boundary condition in the model.  
 220 Wave spectra is obtained from the ocean wave model WAM and is given on a  
 221  $1^\circ \times 1^\circ$  grid with 24 directions and 36 frequencies.

222 Surface waves induce a net drift in the direction of the wave propagation,  
 223 known as the Stokes drift (Van Den Bremer and Breivik, 2018; Stokes,  
 224 1880). This net drift has a significant impact on sediment transport in  
 225 nearshore regions (Hoefel and Elgar, 2003), on the formation of Langmuir  
 226 cells (Langmuir, 1938; Craik and Leibovich, 1976) as well as on the transport  
 227 of heat, salt or pollutants such as oil or micro-plastic in the upper ocean layer  
 228 (McWilliams and Sullivan, 2000; Röhrs et al., 2012; Drivedal et al., 2014). To  
 229 correctly model the Stokes drift profile in mixed wind-driven sea and swell  
 230 conditions, the full two-dimensional wave spectrum must be represented by a  
 231 spectral wave model within a wave-current coupling (Van Den Bremer and  
 232 Breivik, 2018). We therefore used SWAN modeled spectra to compute the  
 233 Stokes drift as follows:

$$\mathbf{u}_s = \int_0^{2\pi} \int_0^{+\infty} \frac{\sigma^3}{h \tanh(2kh)} E(\sigma, \theta) (\cos \theta, \sin \theta) d\sigma d\theta , \quad (6)$$

234 where  $k$  is the norm of the wave vector;  $h$  is the water depth; and  $E(\sigma, \theta)$  is  
 235 the wave energy density.

236    2.5. Coupled model

237    SLIM and SWAN are coupled so that they run on the same computational  
238    core and the same unstructured mesh. SLIM is run first and passes the  
239    wind velocity ( $\mathbf{U}_{10}$ ), water level ( $\eta = H - h$ ) and depth-averaged current  
240    ( $\mathbf{u} = \mathbf{U}/H$ ) fields to SWAN, as well as a roughness length ( $z_0$ ) for the bottom  
241    dissipation formulation of Madsen et al. (1989). This roughness length is  
242    computed from SLIM's bulk drag coefficient  $C_b$  following the approach of  
243    Dietrich et al. (2011) so that both models have consistent bottom dissipation  
244    parameterizations. SWAN then uses these quantities to compute the wave  
245    radiation stress gradient, that is then passed to SLIM as the force exerted  
246    by waves on currents  $\boldsymbol{\tau}_{\text{wave}}$  (Fig. 3). SLIM then uses this quantity to  
247    update the value of the surface stress  $\boldsymbol{\tau}_s$  in Eq. (1), that now becomes  
248    the sum of wind and wave-induced stresses  $\boldsymbol{\tau}_s = \boldsymbol{\tau}_{\text{wind}} + \boldsymbol{\tau}_{\text{wave}}$ . Here, the  
249    momentum flux from the atmosphere to the ocean is taken as the commonly-  
250    used full wind stress  $\boldsymbol{\tau}_{\text{wind}}$ . Doing so, we neglect the momentum advected  
251    away from the storm by the waves, leading to a 10-15% overestimation of the  
252    momentum flux in hurricane winds (Curcic, 2015). Moreover, we followed  
253    the approach of Dietrich et al. (2012) by characterizing the wave-induced  
254    stresses using the radiation-stress representation instead of the vortex-force  
255    representation (McWilliams et al., 2004). Although the latter provides a  
256    clearer and more meaningful decomposition of the wave effect, we implemented  
257    the first representation for the sake of simplicity as it allows us to provide  
258    the whole wave contribution as an additional surface stress to SLIM (Lane  
259    et al., 2007).

260    [Talk a bit more about difference between VF and RS]

261    SLIM's governing equations are integrated using an implicit time inte-  
262    gration scheme while SWAN is unconditionally stable (Dietrich et al., 2012),  
263    allowing both models to be run with relatively large time steps. In this study,  
264    the stationary version of SWAN was used, *i.e.* the first term of Eq. (5) was  
265    set to zero. This resulted in reduced scaling and convergence rates than with

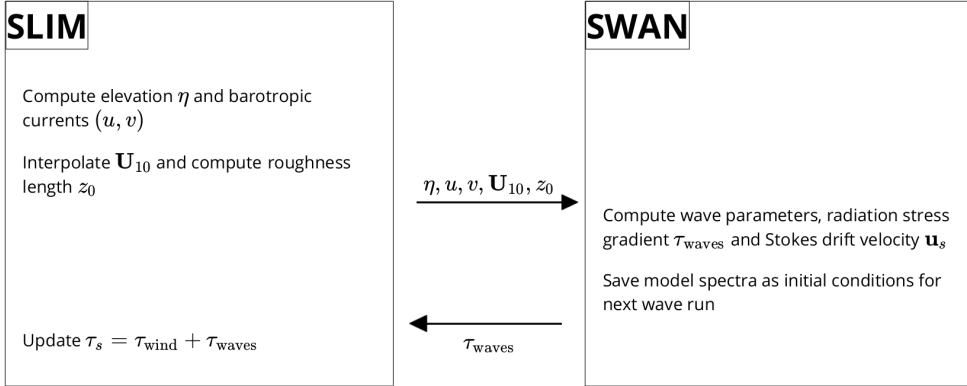


**Fig. 3:** Schematic illustration of the coupled SLIM+SWAN model.

the nonstationary version of SWAN but increased the stability of the model.  
 The wave spectra at each node of the mesh was saved at the end of each iteration to serve as initial conditions for the next one. Both models were run sequentially using a time step of 600 s, so that each computational core was alternatively running either SLIM or SWAN. As in the coupling between SWAN and ADCIRC (Dietrich et al., 2012), both models use the same local sub-mesh, allowing for a one-to-one correspondence between the geographic locations of the mesh vertices. No interpolation is therefore needed when passing the discretised variables from one model to the other, which allows an efficient inter-model communication. However, as SLIM is based on a discontinuous Galerkin finite element method, an additional conversion step to a continuous framework was required to transfer SLIM nodal quantities to SWAN.

#### 2.6. Quantifying the effect of wave-current interactions on transport

To quantify the impact of wave-current interactions on transport processes, we compared the trajectories of passive particles advected by the uncoupled SLIM and coupled SLIM+SWAN currents during the passage of Irma in the Lower Keys. Furthermore, the depth-averaged Stokes drift was computed using the wave spectra of the coupled model SLIM+SWAN run as well as

285 those of an uncoupled SWAN run. Particles were released on the inner and  
286 outer shelves at the points highlighted by red and blue dots in Fig. 4 on  
287 Sept. 7 at 0000 UTC and then tracked until Sept. 15. These initial particle  
288 positions were found using backtracking methods (Spivakovskaya et al., 2005)  
289 to ensure that the release particles would intersect the path of Irma during  
290 its passage through the Florida Keys. We first defined two  $25 \text{ km}^2$  circular  
291 regions on the trajectory of the hurricane (see red and blue circles in Fig. 4).  
292 Particles within these two regions were then tracked backward in time using  
293 uncoupled SLIM currents from the exact time of the passage of the hurricane  
294 until Sept. 7 at 0000 UTC. Their positions at the end of the backward  
295 simulation (see red and blue particle clouds in Fig. 4) corresponds to the  
296 initial condition of the forward transport simulations described below. We  
297 then compared the trajectories of particles originating from these regions and  
298 advected forward in time by different sets of currents: (i) uncoupled SLIM  
299 currents alone; (ii) coupled SLIM+SWAN currents; (iii) SLIM currents with  
300 the addition of the depth-averaged Stokes drift computed with the coupled  
301 wave-current model (Stokes-C); (iv) SLIM+SWAN currents with Stokes-C;  
302 and (v) SLIM currents with the depth-averaged Stokes drift computed with  
303 the uncoupled wave model (Stokes-U). Particle trajectories are compared by  
304 computing the distances between the centers of mass of the particle clouds  
305 through time.

### 306 3. Results

307 We first validated the reconstructed atmospheric fields of hurricane Irma  
308 as well as the outputs of our coupled wave-current model against field measure-  
309 ments. We then used the validated model outputs to simulate the transport  
310 of passive particles in the Lower Keys during the passage of Hurricane Irma.  
311 These particles were advected by the sets of currents described in section  
312 2.6 and their trajectories were compared to evaluate the impact of the wave-  
313 current interactions and the Stokes drift on the transport processes during

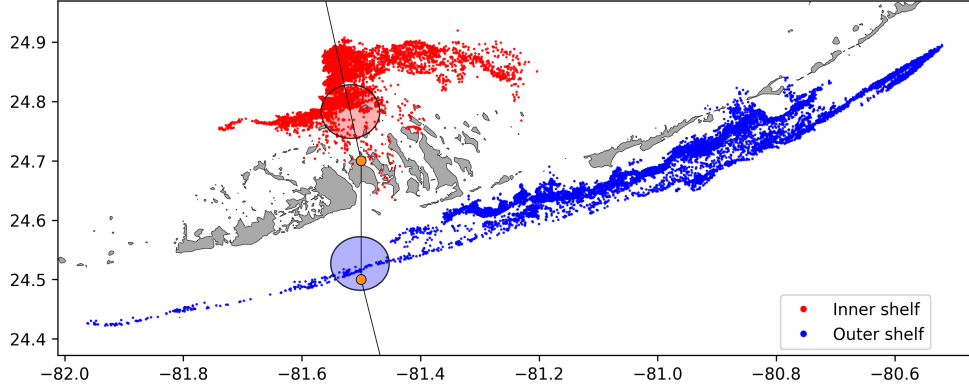


**Fig. 4:** Release regions of the passive particles on the inner and outer shelves (red and blue clouds) obtained by backtracking particles released in the red and blue circular areas during the passage of Irma.

314 the passage of Irma.

315 *3.1. Model validation*

316 H\*Wind winds and hybrid pressure field agree well with station mea-  
 317 surements at Vaca Key station (Fig. 5). The hybrid pressure field shows a  
 318 better agreement with observations than ERA-5 pressure as it successfully  
 319 reproduces the storm depression. ERA-5 fields, on the other hand, fail to  
 320 reproduce the low pressure at the core of the hurricane due to their coarser  
 321 grid, leading to an overestimation of 8 mbar of the storm depression. Both  
 322 H\*Wind and ERA-5 agree well with observed wind speeds although both  
 323 data sets tend to slightly overestimate the width and intensity of the wind  
 324 peak. However, H\*Wind profiles better reproduce the timing of the observed  
 325 peak, as ERA-5 winds tend to anticipate it. H\*wind also exhibits a slightly  
 326 narrower peak in wind speed, which better agrees with observations.

327 Hydrodynamic outputs of the coupled wave-current model agree well  
 328 with tide gauge (Fig. 6) and ADCP measurements (Fig. 7). Despite a  
 329 slight overestimation of the amplitude of sea surface elevation in fair weather  
 330 conditions, the timing and amplitude of the storm surges are well reproduced  
 331 by the coupled model. The largest model error during the surge is an

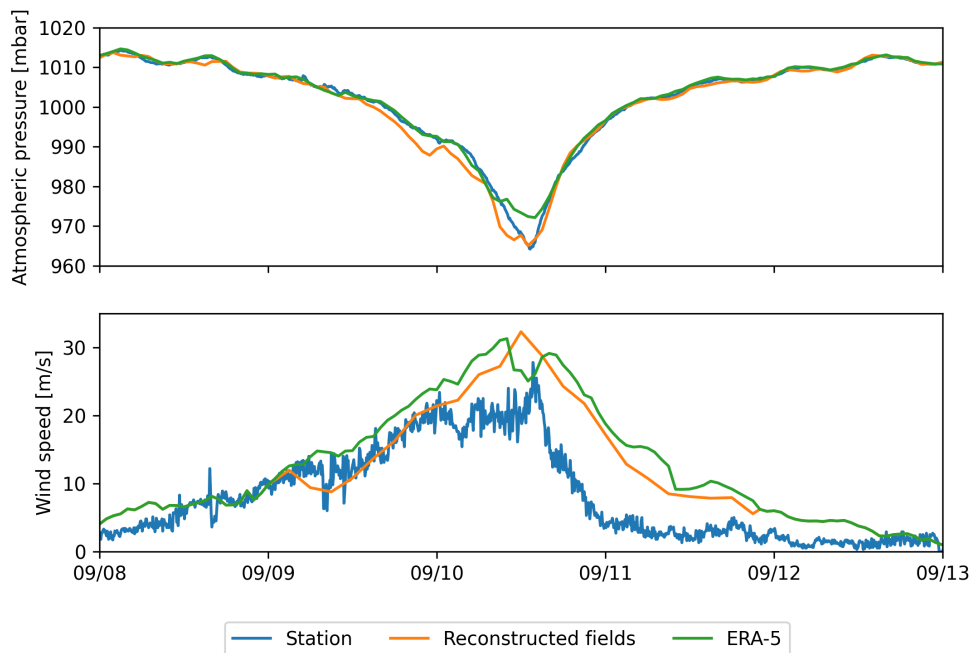


**Fig. 5:** Comparison of reconstructed wind (top) and atmospheric pressure (bottom) with field measurements and coarser ECMWF ERA-5 profiles at Vaca Key station. The generated hybrid atmospheric forcings better reproduce the observed storm depression while H\*wind winds better reproduce the measured peak in wind speed.

332 overestimation of 18 cm of the elevation peak at Virginia Key. The fit is  
333 especially good at Naples, where both the large positive and negative surges  
334 are captured by the coupled model with an error of less than 5 cm. Modeled  
335 2D currents were validated against depth-averaged ADCP measurements  
336 at mooring stations C10 (Fig. 7), C12 and C13. As in Liu et al. (2020),  
337 we performed the vector correlation analysis of Kundu (1976) to compare  
338 modeled and observed current velocity vectors. Correlation coefficients ( $\rho$ )  
339 between simulated and observed depth-averaged currents are 0.84, 0.74 and  
340 0.73 at stations C10, C12 and C13, respectively. The average veering angles  
341 are below 12°, as in (Liu et al., 2020). Furthermore, the positive bias in Table  
342 1 indicates that our model tends to underestimate the southward component  
343 of the currents at the different stations. As expected from a depth-averaged  
344 model, the best fit with observations is obtained at the shallowest mooring  
345 C10, located on the 25 m isobath, with an average veering angle of 6° and  
346 smaller error statistics (Table 1).

347 The simulated significant wave height agrees well with observations on the  
348 WFS (buoys 41113 and 41114), where errors on the peak value do not exceed  
349 5% (Fig. 8). On Florida's eastern shelf (buoys 42036 and 42097), errors  
350 are slightly larger and reach 20%. Although the model outputs agree well  
351 with observations, a lag in significant wave height is observed for all 4 buoys.  
352 Moreover, the peak in significant wave height tends to be underestimated at  
353 buoys 41113 and 41114, located on the eastern shelf of Florida. The same  
354 tendency is observed with the modeled wave period, with mean errors inferior  
355 to 1 second on the WFS and reaching more than 2 seconds on Florida's  
356 eastern shelf (Table 1), as the coupled model fails to reproduce the observed  
357 peak in wave period between the 7th and 8th of September on this side of  
358 Florida. Finally, modeled wave direction agrees well with observation (Fig. 8),  
359 although our model tends to overestimate wave propagation in the northward  
360 direction at stations 41114 and 41113 on the passage of the hurricane (not  
361 shown).

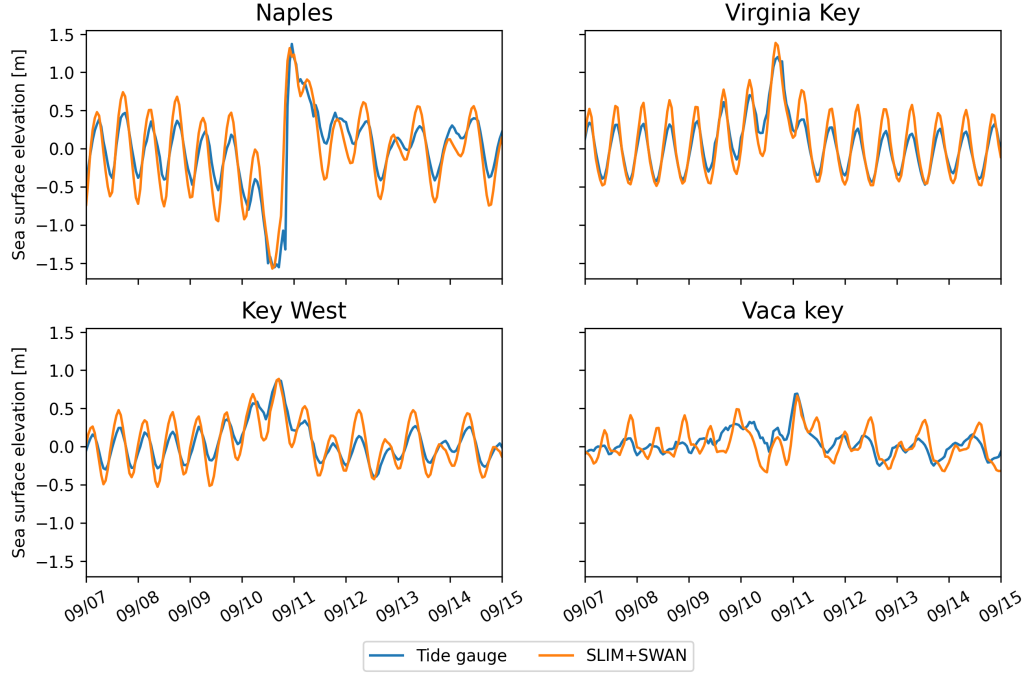


**Fig. 6:** Comparison of modeled sea surface elevation at the 4 tide gauges shown in Fig. 1B. The timing and amplitude of the storm surges are well reproduced by the model

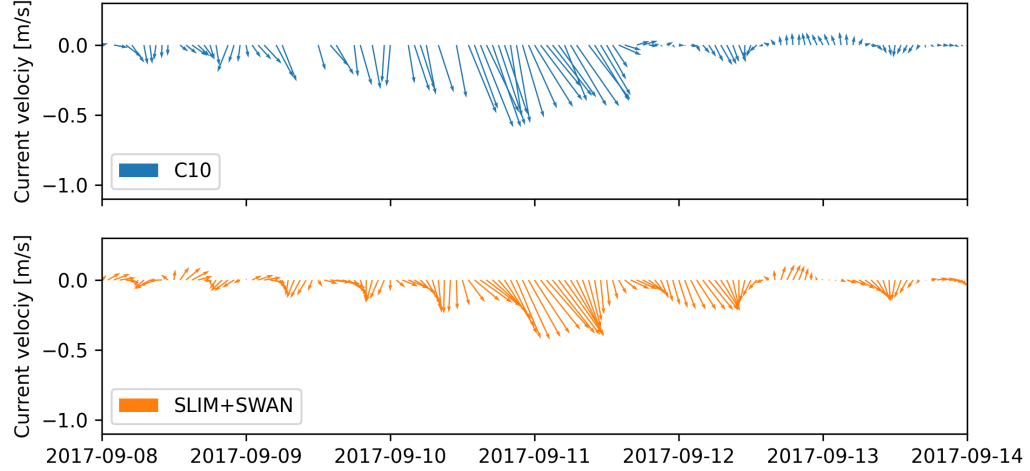


**Fig. 7:** Comparison of modeled current velocity with observed velocity at mooring C10 (see Fig. 1B for its location). Modeled current velocities agree well with observations, with a correlation coefficient of 0.84 and an average veering angle of 6°.

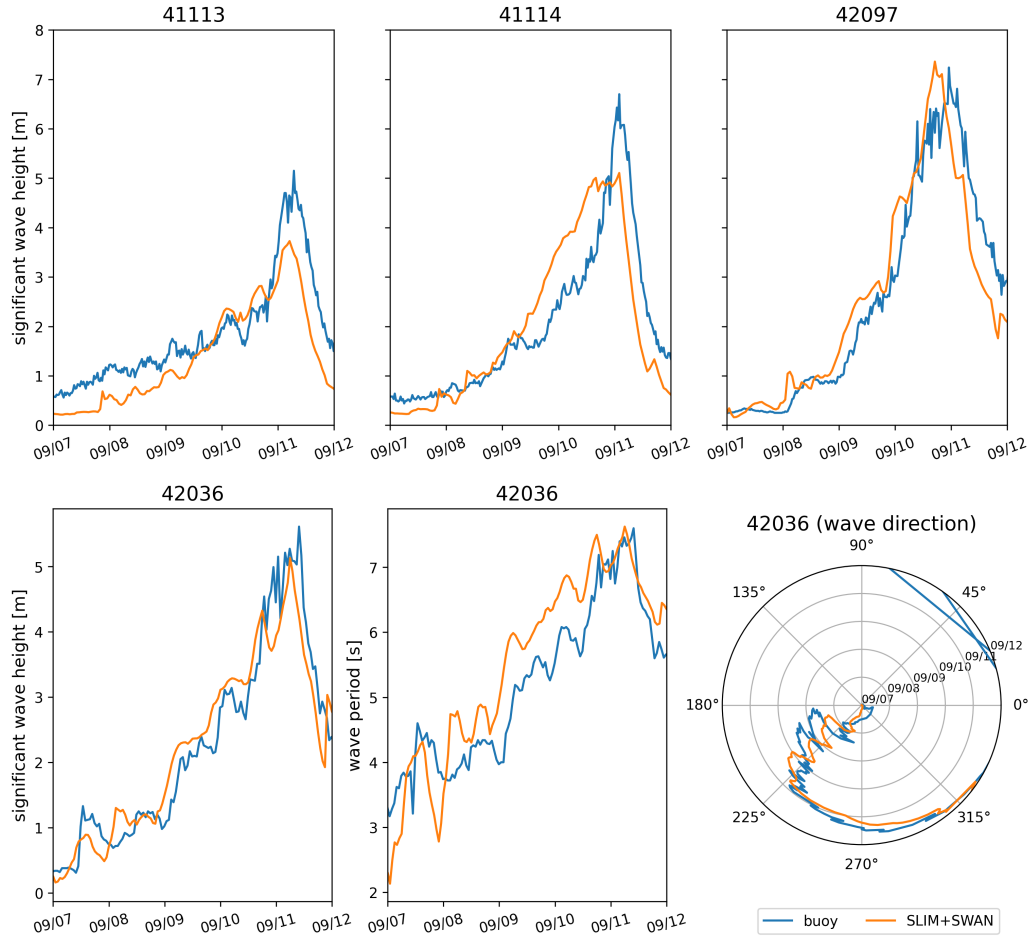


**Fig. 8:** Comparison of modeled wave parameters with observation at the 4 buoys location (locations shown in Fig. 1B). The modeled significant wave heights agree well with field measurement.

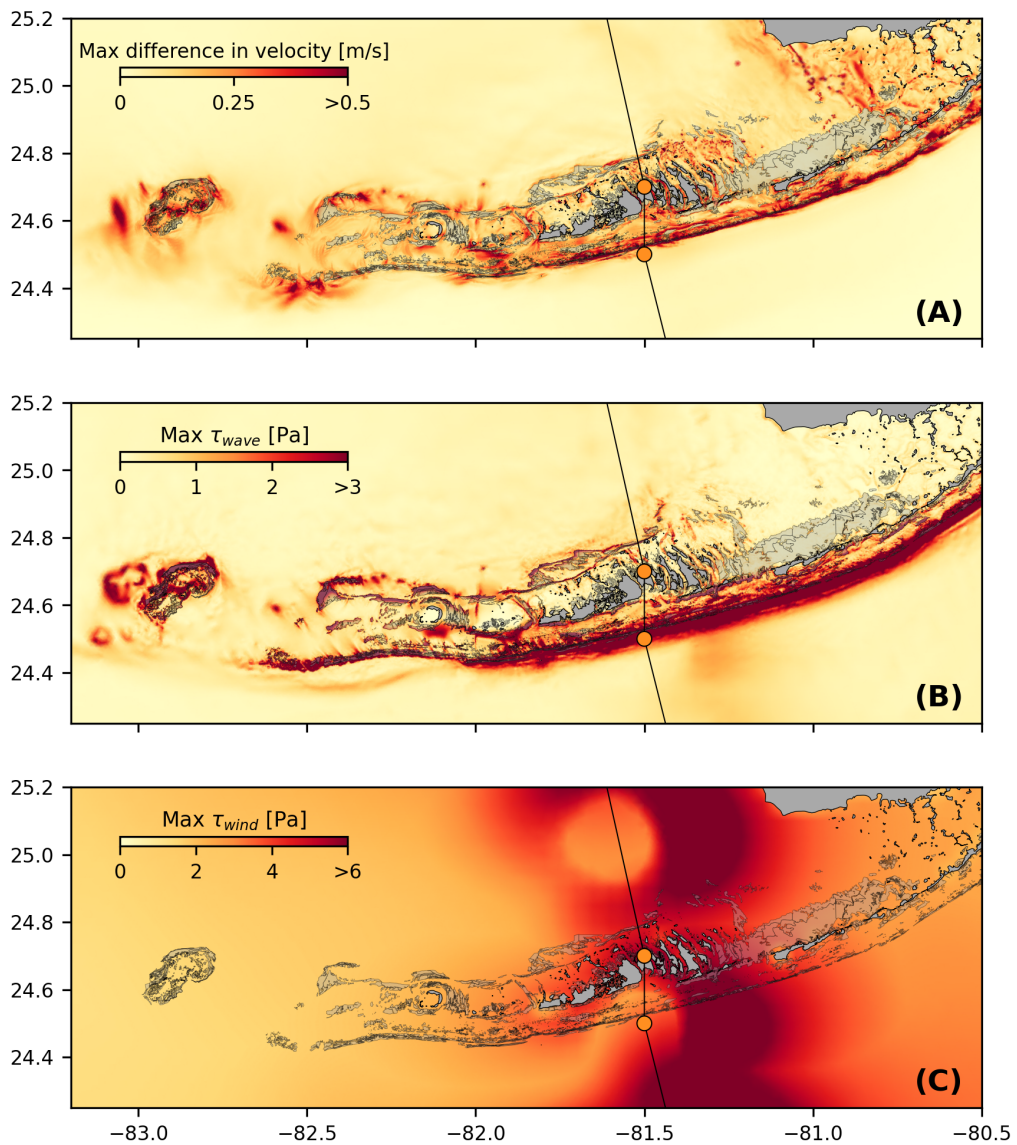
<b>Station</b>	<b>Variable</b>	<b>Bias</b>	<b>MAE</b>	<b>RMSE</b>
Vaca Key	sse (m)	n/a	0.12	0.16
	$U_{10}$ (m/s)	1.51	1.85	2.61
	$p_{atm}$ (hPa)	-0.21	0.59	1.03
Key West	sse (m)	n/a	0.11	0.13
Virginia Key	sse (m)	n/a	0.10	0.13
Naples	sse (m)	n/a	0.18	0.23
C10	$u$ (m/s)	-0.006	0.04	0.05
	$v$ (m/s)	0.02	0.06	0.08
C12	$u$ (m/s)	-0.01	0.06	0.07
	$v$ (m/s)	0.06	0.09	0.11
C13	$u$ (m/s)	0.004	0.06	0.08
	$v$ (m/s)	0.04	0.06	0.08
41113	$H_s$ (m)	-0.35	0.40	0.51
	$T_m$ (s)	-2.18	2.47	3.13
	$\theta_m$ (degree)	7.17	19.50	26.06
41114	$H_s$ (m)	-0.21	0.53	0.68
	$T_m$ (s)	-1.69	2.53	3.15
	$\theta_m$ (degree)	31.25	35.28	46.18
42036	$H_s$ (m)	-0.03	0.26	0.36
	$T_m$ (s)	0.04	0.65	0.77
	$\theta_m$ (degree)	19.92	30.65	41.69
42097	$H_s$ (m)	-0.15	0.40	0.57
	$T_m$ (s)	0.02	0.62	0.74
	$\theta_m$ (degree)	3.62	28.08	45.89

Table 1: Error statistics on the wave-current model outputs as compared to the measured sea surface elevation (sse), eastward and northward depth-average current velocities ( $u,v$ ), significant wave height ( $H_s$ ), zero-crossing mean wave period ( $T_m$ ) and mean wave direction ( $\theta_m$ ). Model bias, mean absolute error (MAE), and root mean squared error (RMSE) are listed by variable (unit) and value.

362     *3.2. Impact of waves on currents and transport*

363     We evaluated the impact of wave-current interactions on modeled currents  
364     during the passage of Irma in the Lower Keys, between Sept. 7 and 13, 2017.  
365     First, we computed the maximum difference between currents modeled by  
366     SLIM and SLIM+SWAN during this period (Fig. 9A). The largest differences  
367     in current speed were observed over the reefs, on the shelf break and around  
368     islands. They locally reach 1 m/s, with the coupled SLIM+SWAN model  
369     yielding the largest amplitudes. The regions where the differences are the  
370     largest experience the strongest radiation-stress gradient  $\tau_{\text{wave}}$  (Fig. 9B)  
371     induced by wave energy dissipation on the shelf-break and rough seabed  
372     induce variations of the wave radiation stress (Longuet-Higgins and Stewart,  
373     1964). This highlights the important protective role of the barrier formed  
374     by the offshore reefs, that require a fine spatial resolution to be accurately  
375     captured. Wave-induced differences in current speed were amplified by the  
376     action of the wind stress  $\tau_{\text{wind}}$  (Fig. 9C). Wind speeds were larger in the front  
377     right quadrant of the hurricane (Zedler et al., 2009), yielding larger differences  
378     on the right-hand side of the storm trajectory. This is especially clear in the  
379     area between the Florida Keys and the Everglades, where relatively small  
380     values of  $\tau_{\text{wave}}$  nonetheless produce current speed differences of up to 0.5 m/s  
381     because of the wind stress.

382     Waves play a significant role on the transport processes during and after the  
383     passage of hurricane Irma (Fig. 10A,B). Comparing SLIM and SLIM+SWAN  
384     shows that wave-current interactions alone yield differences of up to 5 km  
385     between the modeled trajectories on the passage of the hurricane. These  
386     differences exceed 10 km on the outer shelf when Stokes drift is taken into  
387     account. Such deflections are not negligible when compared to the total  
388     distance traveled by particle clouds. For all simulations, modeled particles  
389     were transported up to 30 km from their release point on the inner shelf  
390     and up to 60 km on the outer shelf. The impact of the waves on the  
391     transport processes differs significantly between the inner and outer shelves,



**Fig. 9:** (A). Maximum difference between SLIM and SLIM+SWAN currents during the passage of Irma in the Lower Florida Keys; (B) Maximum wave radiation stress gradient  $\tau_{wave}$  and (C) maximum wind stress  $\tau_{wind}$  (C) generated by the hurricane. Radiation stress gradient yields difference larger than 0.5 m/s (and locally reaching 1m/s) in current velocities, especially over offshore reefs.

392 with wave-induced differences in trajectories 4 to 5 times larger on the outer  
393 shelf. Furthermore, the distance between the centers of mass of the clouds  
394 of particles tends to stabilize on the inner shelf after the passage of Irma,  
395 while it keeps increasing on the outer shelf up to two days after the passage  
396 of the hurricane when taking Stokes drift into account. The distance then  
397 stabilizes for about a day before it starts decreasing (see right panel of Fig.  
398 10A,B). However, when considering wave-current interactions alone (SLIM  
399 vs. SLIM+SWAN), the distance between the clouds of particles starts to  
400 decrease just after the passage of Irma.

401 The Stokes drift appears to have a larger effect than the radiation stress  
402 gradient and the wave-current interactions (Fig 10A,B). Nonetheless, compar-  
403 ing the different curves for the outer shelf suggests that the radiation-stress  
404 gradient induces effects similar to the impact of the Stokes drift in this  
405 region during the passage of Irma. However, when comparing SLIM and  
406 SLIM+SWAN both on the inner and outer shelf, this impact appears to be  
407 negligible during the rest of the simulation. Comparing Stokes-U and Stokes-C  
408 indicates that the difference between the trajectories of particles advected by  
409 the two Stokes drifts does not exceed 2 km, with larger discrepancies on the  
410 outer shelf (Fig. 10C,D). The distance between the two clouds of particles  
411 increases abruptly on the passage of the hurricane (and two days after on the  
412 outer shelf) and then stabilizes during the rest of the simulation.

#### 413 4. Discussion

414 The coupled SLIM+SWAN model correctly reproduces the hydrodynamics  
415 and wave dynamics during hurricane Irma. Such good agreement with field  
416 measurements can only be achieved using accurate forcings and adequate  
417 wave parameterizations. By comparing coupled and uncoupled model runs, we  
418 showed that neglecting wave radiation stress gradient can induce differences  
419 of up to 1 m/s in modeled current velocities. The radiation stress gradient  
420 during the hurricane was especially large over the shelf break, where waves

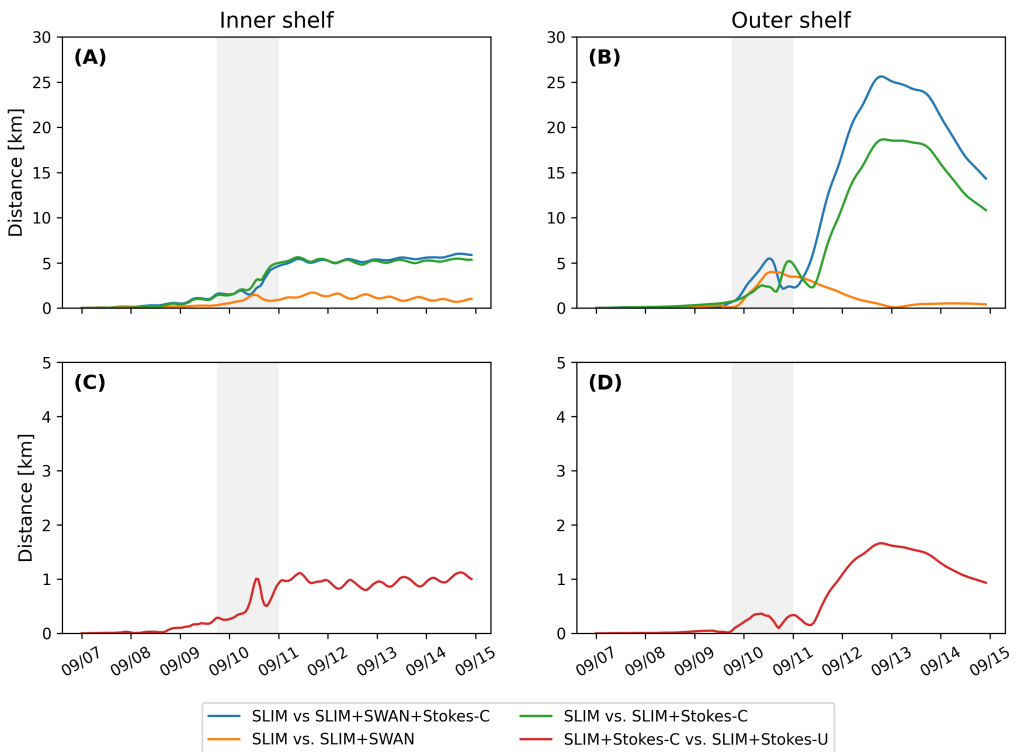


**Fig. 10:** Difference between the centers of mass of the particle clouds released from the regions highlighted in Fig. 4 and advected by different combinations of coupled and uncoupled velocity fields.

421 are strongly dissipated by the offshore coral reef barrier. The radiation stress  
422 gradient alone can deflect drifting particles by up to 5 km during the passage  
423 of the hurricane. These differences in modeled trajectories were significantly  
424 larger and required more time to stabilize on the outer shelf. The impact of  
425 the Stokes drift dominates the effects of wave-current interactions through the  
426 radiation stress gradient, except during the passage of the hurricane, when  
427 both contributions are similar. Finally, neglecting wave-current interactions  
428 when computing Stokes drift leads to variations of up to 2 km in modeled  
429 trajectories on the passage of the hurricane.

430 Despite slightly overestimating the amplitude of the sea surface elevation in  
431 fair weather conditions, the coupled wave-current model correctly reproduces  
432 the timing and amplitude of the observed storm surge. All elevation peaks are  
433 captured with a 4% accuracy at every station except Virginia key, where the  
434 surge was overestimated by about 15%. Such accuracy is key to predict the  
435 damages caused by the hurricane, as most destroyed and severely damaged  
436 buildings in the Florida Keys during Hurricane Irma were caused by storm  
437 surge and waves (Xian et al., 2018). Furthermore, by using a high-resolution  
438 model, we can explicitly reproduce the circulation between all the reefs and  
439 islands of the Florida Keys. The fine-scale details of the storm surge, and  
440 hence the associated risk, are thus accurately represented. In addition to  
441 accurately capturing positive surges, the model also reproduced the observed  
442 negative surge in Naples with an error of about 1%. This result is of interest  
443 from a biological point of view as negative surges, although less studied, affect  
444 water exchanges between the estuaries and the coastal ocean and disturb  
445 the benthic ecosystems (Liu et al., 2020). Such rapid decrease in water  
446 level followed by a positive surge cause massive freshwater inflows, causing a  
447 significant decrease in water salinity (Wachnicka et al., 2019).

448 Strong currents such as the Gulf Stream affect waves trough refraction  
449 over gradients in current velocity, shoaling and breaking of opposing waves or  
450 lengthening of following waves (Hegermiller et al., 2019). Under hurricane

451 conditions, these interactions can cause numerical instabilities in the wave  
452 model if the parameterizations are not appropriate and the model resolution  
453 not sufficient. Hegermiller et al. (2019), for instance, used a 5-km model  
454 grid and 48 directional bins to capture spatial gradients in wave height  
455 induced by wave-currents interactions in the Gulf Stream during Hurricane  
456 Matthew (2016). We followed these guidelines when defining the coarsest  
457 resolution of the model mesh as well as the spectral discretization of SWAN.  
458 Boundary conditions and directional spreading of the incident waves also  
459 play a significant role when modeling wave-current interactions at meso-  
460 and submesoscales (Villas Bôas et al., 2020), which motivated our choice  
461 of imposing full spectra on the boundary of the wave model instead of  
462 bulk parameters. Finally, SWAN default parameterizations for wind energy  
463 input and whitecapping caused numerical instabilities by overestimating wave  
464 growth and steepness on the boundary of the Gulf Stream on the passage  
465 of Irma. This overestimation was solved by using the parameterization of  
466 Siadatmousavi et al. (2011). The parameters used in this study were calibrated  
467 on the Northern Gulf of Mexico conditions, which might explain that our  
468 model better reproduces wave parameters at buoys located on the WFS.  
469 However, these calibrated parameters might underestimate wind-induced  
470 wave growth on Florida's eastern shelf. Consequently, incident wave do not  
471 receive enough energy to grow after breaking on the bank boundary, leading to  
472 an underestimation of the significant wave height at buoys located on Florida's  
473 eastern shelf. A more extensive calibration study might therefore be necessary  
474 to further improve the agreement with field measurements on both sides of  
475 Florida. Nonetheless, as this study focuses on the wave produced by Irma,  
476 which made landfall on the West coast of Florida, the use of parameterizations  
477 calibrated for the Gulf of Mexico seems reasonable.

478 The radiation stress gradient significantly impacts currents during the  
479 passage of the hurricane. It can induce differences of up to 1 m/s in the  
480 current speed on the shelf break. In this region waves are strongly dissipated

481 due to action of depth-induced breaking and bottom dissipation on coral reefs.  
482 This highlights the protective role of coral reefs against strong incoming waves  
483 (Lowe et al., 2005), which requires a sufficiently fine spatial resolution to be  
484 explicitly represented in the model. Due to the dissipation of incoming waves  
485 on the reefs, wave impact during Irma is different on the inner and outer  
486 shelves. It is less important on the inner shelf because of the sheltering of the  
487 inner shelf due to reefs and islands as well as wave breaking on the shelf break.  
488 The inner shelf hence experiences weaker waves and currents, inducing weaker  
489 and more localized transport. Furthermore, the impact of winds on waves  
490 is reduced in shallower areas under the action of depth-induced breaking.  
491 This might explain why differences between particle trajectories stabilize  
492 on the inner shelf just after the passage of Hurricane Irma. However, the  
493 Florida Keys still experienced strong winds after the passage of the core of  
494 the hurricane, which generated high waves in the deeper areas. This might  
495 explain why the differences between the modeled trajectories kept increasing  
496 on the outer shelf under the action of strong Stokes drift up to two days after  
497 the passage of the hurricane.

498 The distance between the centers of mass of the particle clouds advected  
499 by coupled and uncoupled Stokes drift remains rather limited (< 2 km). This  
500 suggests that taking wave-current interactions into account when computing  
501 Stokes drift, even in heavy wind conditions has a limited impact. Furthermore,  
502 combining the coupled Stokes drift with the coupled and uncoupled SLIM  
503 currents produced similar trajectories on the inner shelf, which seems to  
504 indicate that wave impact on currents is limited in this region. This would  
505 suggest that it is not necessary to take wave-current interactions into account  
506 when modeling the trajectories of tracers in shallow, sheltered areas such  
507 as the inner WFS during a hurricane. Uncoupled currents with uncoupled  
508 Stokes drift should give a reasonably accurate approximation of the transport  
509 processes. However, this does not hold for deeper and unsheltered regions,  
510 as highlighted by the comparison of trajectories obtained with coupled and

511 uncoupled SLIM currents combined with coupled Stokes drift on the outer  
512 shelf.

513 **5. Conclusion**

514 We developed a coupled wave-current model to study the impact of waves  
515 on transport processes during Hurricane Irma. In order to accurately represent  
516 the wind and pressure profiles of the hurricane, we built hybrid fields by  
517 combining coarser ERA-5 data with high-resolution H\*Wind data for the wind  
518 speed and idealized Holland profiles for the pressure. Comparing these hybrid  
519 profiles with field observations showed that they were better at reproducing the  
520 observed central depression of the hurricane as well as the peak in wind speed  
521 than ERA-5 data. Using these hybrid fields as forcings, our coupled model  
522 accurately reproduced the storm surge at tide gauge locations and produced  
523 currents and wave parameters in good agreement with field observations,  
524 especially on the West Florida Shelf. The modeled currents and Stokes drift  
525 were then used to evaluate the impact of waves on the trajectory of passive  
526 drifters on the passage of the hurricane through the Florida Keys. Our results  
527 show that waves had a significant impact on heavy-wind transport processes  
528 and caused deflections of the drifters trajectories by more than 20 km on the  
529 outer shelf.

530 Despite its good agreement with observations, our model could be fur-  
531 ther refined by improving the representation of wind-wave interactions. In  
532 particular, it does not consider the momentum loss due to the action of  
533 surface waves when representing momentum flux from the atmosphere to the  
534 ocean, leading to overestimations under hurricane conditions. Our model  
535 could therefore be further improved by using wave-dissipative stress instead  
536 of the full wind stress as the momentum flux from the atmosphere to the  
537 ocean. Moreover, a more thorough calibration of the wave model parameters  
538 should improve our model results on Florida's eastern shelf. Finally, as a 2D  
539 barotropic model, SLIM does not explicitly represent baroclinic phenomenons

540 as well as the vertical profile of the Stokes drift and radiation stress gradient  
541 along the wave boundary layer. However, our study focused on relatively  
542 shallow and vertically homogeneous coastal waters using a reef-scale resolution  
543 throughout the whole FRT. Such fine resolution allows to explicitly represent  
544 wave dissipation over coral reefs and is only achievable using a 2D model due  
545 to computational resource limitations.

546 Wave coupling needs to be taken into account during heavy-wind events  
547 but not necessarily in milder conditions. While the radiation stress gradient  
548 plays an important role and can lead to differences of up to 5 km, the  
549 Stokes drift is about 4 times more intense and should thus be considered  
550 in priority. This study brings new insight on the impact of waves on the  
551 transport processes nearshore during a tropical cyclone. Due to its high  
552 spatial resolution, the developed coupled wave-current model can be used  
553 to accurately represent the dispersal of pollutants, sediments or larvae in  
554 topologically complex coastal areas in heavy-wind conditions.

## 555 Acknowledgments

556 Computational resources were provided by the Consortium des Équipements  
557 de Calcul Intensif (CÉCI), funded by the F.R.S.-FNRS under Grant No.  
558 2.5020.11. Thomas Dobbelaere is a PhD student supported by the Fund for  
559 Research training in Industry and Agriculture (FRIA/FNRS).

560 This work was also supported by the Disaster Related Appropriation  
561 Supplemental: Improving Forecasting and Assimilation (DRAS 19 IFAA),  
562 awarded to the University of Miami under award NA19OAR0220184. It was  
563 also supported by the FY19 Disaster Supplemental: Improving Forecasting of  
564 Hurricanes, Floods, and Wildfires (FY19 IFHFW) awarded to the University  
565 of Miami under award NA20OAR4600263. M. Le Hénaff received partial  
566 support for work on this publication by NOAA/AOML, and was partly  
567 supported under the auspices of the Cooperative Institute for Marine and  
568 Atmospheric Studies (CIMAS), a cooperative institute of the University of

569 Miami and NOAA, cooperative agreement NA20OAR4320472.

570 **References**

- 571 Abdolali, A., Roland, A., Van Der Westhuysen, A., Meixner, J., Chawla,  
572 A., Hesser, T.J., Smith, J.M., Sikiric, M.D., 2020. Large-scale hurricane  
573 modeling using domain decomposition parallelization and implicit scheme  
574 implemented in WAVEWATCH III wave model. Coastal Engineering 157,  
575 103656.
- 576 Bever, A.J., MacWilliams, M.L., 2013. Simulating sediment transport pro-  
577 cesses in San Pablo Bay using coupled hydrodynamic, wave, and sediment  
578 transport models. Marine Geology 345, 235–253.
- 579 Bhatia, K.T., Vecchi, G.A., Knutson, T.R., Murakami, H., Kossin, J., Dixon,  
580 K.W., Whitlock, C.E., 2019. Recent increases in tropical cyclone intensifi-  
581 cation rates. Nature Communications 10, 1–9.
- 582 Booij, N., Ris, R.C., Holthuijsen, L.H., 1999. A third-generation wave  
583 model for coastal regions: 1. Model description and validation. Journal of  
584 Geophysical Research: Oceans 104, 7649–7666.
- 585 Breivik, Ø., Allen, A.A., Maisondieu, C., Olagnon, M., 2013. Advances in  
586 search and rescue at sea. Ocean Dynamics 63, 83–88.
- 587 Cangialosi, J.P., Latto, A.S., Berg, R., 2018. National Hurricane Center  
588 Tropical Cyclone Report: Hurricane Irma (30 August12 September 2017).  
589 [https://www.nhc.noaa.gov/data/tcr/AL112017\\_Irma.pdf](https://www.nhc.noaa.gov/data/tcr/AL112017_Irma.pdf).
- 590 Chassignet, E.P., Hurlbert, H.E., Smedstad, O.M., Halliwell, G.R., Hogan,  
591 P.J., Wallcraft, A.J., Baraille, R., Bleck, R., 2007. The HYCOM (hybrid  
592 coordinate ocean model) data assimilative system. Journal of Marine  
593 Systems 65, 60–83.

- 594 Craik, A.D., Leibovich, S., 1976. A rational model for Langmuir circulations.  
595 Journal of Fluid Mechanics 73, 401–426.
- 596 Curcic, M., 2015. Explicit air-sea momentum exchange in coupled atmosphere-  
597 wave-ocean modeling of tropical cyclones. Ph.D. thesis. University of Miami.
- 598 Curcic, M., Chen, S.S., Özgökmen, T.M., 2016. Hurricane-induced ocean  
599 waves and stokes drift and their impacts on surface transport and dispersion  
600 in the Gulf of Mexico. Geophysical Research Letters 43, 2773–2781.
- 601 Curcic, M., Haus, B.K., 2020. Revised estimates of ocean surface drag in  
602 strong winds. Geophysical Research Letters 47, e2020GL087647.
- 603 Dietrich, J., Bunya, S., Westerink, J., Ebersole, B., Smith, J., Atkinson,  
604 J., Jensen, R., Resio, D., Luettich, R., Dawson, C., et al., 2010. A high-  
605 resolution coupled riverine flow, tide, wind, wind wave, and storm surge  
606 model for southern Louisiana and Mississippi. Part II: Synoptic description  
607 and analysis of Hurricanes Katrina and Rita. Monthly Weather Review  
608 138, 378–404.
- 609 Dietrich, J., Westerink, J., Kennedy, A., Smith, J., Jensen, R., Zijlema, M.,  
610 Holthuijsen, L., Dawson, C., Luettich, R., Powell, M., et al., 2011. Hurricane  
611 Gustav (2008) waves and storm surge: Hindcast, synoptic analysis, and  
612 validation in southern Louisiana. Monthly Weather Review 139, 2488–2522.
- 613 Dietrich, J.C., Tanaka, S., Westerink, J.J., Dawson, C., Luettich, R., Zijlema,  
614 M., Holthuijsen, L.H., Smith, J., Westerink, L., Westerink, H., 2012. Per-  
615 formance of the unstructured-mesh, SWAN+ ADCIRC model in computing  
616 hurricane waves and surge. Journal of Scientific Computing 52, 468–497.
- 617 Dobbelaere, T., Muller, E.M., Gramer, L.J., Holstein, D.M., Hanert, E., 2020.  
618 Coupled epidemic-hydrodynamic modeling to understand the spread of a  
619 deadly coral disease in Florida. Frontiers in Marine Science 7, 1016.

- 620 Donelan, M., Haus, B., Reul, N., Plant, W., Stiassnie, M., Gruber, H., Brown,  
621 O., Saltzman, E., 2004. On the limiting aerodynamic roughness of the  
622 ocean in very strong winds. *Geophysical Research Letters* 31.
- 623 Drivdal, M., Broström, G., Christensen, K., 2014. Wave-induced mixing and  
624 transport of buoyant particles: Application to the Statfjord A oil spill.  
625 *Ocean Science* 10, 977–991.
- 626 Figueiredo, J., Baird, A.H., Connolly, S.R., 2013. Synthesizing larval com-  
627 petence dynamics and reef-scale retention reveals a high potential for  
628 self-recruitment in corals. *Ecology* 94, 650–659.
- 629 Fringer, O.B., Dawson, C.N., He, R., Ralston, D.K., Zhang, Y.J., 2019. The  
630 future of coastal and estuarine modeling: Findings from a workshop. *Ocean*  
631 *Modelling* 143, 101458.
- 632 Frys, C., Saint-Amand, A., Le Hénaff, M., Figueiredo, J., Kuba, A., Walker,  
633 B., Lambrechts, J., Vallaeyns, V., Vincent, D., Hanert, E., 2020. Fine-scale  
634 coral connectivity pathways in the Florida Reef Tract: Implications for  
635 conservation and restoration. *Frontiers in Marine Science* 7, 312.
- 636 Geuzaine, C., Remacle, J.F., 2009. Gmsh: A 3-d finite element mesh generator  
637 with built-in pre-and post-processing facilities. *International journal for*  
638 *numerical methods in engineering* 79, 1309–1331.
- 639 Harper, B., Kepert, J., Ginger, J., 2010. Guidelines for converting between  
640 various wind averaging periods in tropical cyclone conditions.
- 641 Hegermiller, C.A., Warner, J.C., Olabarrieta, M., Sherwood, C.R., 2019.  
642 Wave-current interaction between Hurricane Matthew wave fields and the  
643 Gulf Stream. *Journal of Physical Oceanography* 49, 2883–2900.
- 644 Hoefel, F., Elgar, S., 2003. Wave-induced sediment transport and sandbar  
645 migration. *Science* 299, 1885–1887.

- 646 Holthuijsen, L.H., Powell, M.D., Pietrzak, J.D., 2012. Wind and waves in  
647 extreme hurricanes. *Journal of Geophysical Research: Oceans* 117.
- 648 Janssen, P.A., 1991. Quasi-linear theory of wind-wave generation applied to  
649 wave forecasting. *Journal of Physical Oceanography* 21, 1631–1642.
- 650 Johns, W.E., Schott, F., 1987. Meandering and transport variations of the  
651 Florida Current. *Journal of Physical Oceanography* 17, 1128–1147.
- 652 Knaff, J.A., Sampson, C.R., Musgrave, K.D., 2018. Statistical tropical cyclone  
653 wind radii prediction using climatology and persistence: Updates for the  
654 western North Pacific. *Weather and Forecasting* 33, 1093–1098.
- 655 Knutson, T., Camargo, S.J., Chan, J.C., Emanuel, K., Ho, C.H., Kossin, J.,  
656 Mohapatra, M., Satoh, M., Sugi, M., Walsh, K., et al., 2020. Tropical  
657 cyclones and climate change assessment: Part II: Projected response to  
658 anthropogenic warming. *Bulletin of the American Meteorological Society*  
659 101, E303–E322.
- 660 Komen, G., Hasselmann, S., Hasselmann, K., 1984. On the existence of a  
661 fully developed wind-sea spectrum. *Journal of Physical Oceanography* 14,  
662 1271–1285.
- 663 Kossin, J.P., Knapp, K.R., Olander, T.L., Velden, C.S., 2020. Global increase  
664 in major tropical cyclone exceedance probability over the past four decades.  
665 *Proceedings of the National Academy of Sciences* 117, 11975–11980.
- 666 Kourafalou, V.H., Kang, H., 2012. Florida Current meandering and evo-  
667 lution of cyclonic eddies along the Florida Keys Reef Tract: Are they  
668 interconnected? *Journal of Geophysical Research: Oceans* 117.
- 669 Kundu, P.K., 1976. Ekman veering observed near the ocean bottom. *Journal*  
670 *of Physical Oceanography* 6, 238–242.

- 671 Lambrechts, J., Hanert, E., Deleersnijder, E., Bernard, P.E., Legat, V.,  
672 Remacle, J.F., Wolanski, E., 2008. A multi-scale model of the hydrodynamics  
673 of the whole Great Barrier Reef. *Estuarine, Coastal and Shelf Science*  
674 79, 143–151.
- 675 Landsea, C.W., Franklin, J.L., 2013. Atlantic hurricane database uncertainty  
676 and presentation of a new database format. *Monthly Weather Review* 141,  
677 3576–3592.
- 678 Lane, E.M., Restrepo, J., McWilliams, J.C., 2007. Wave–current interaction:  
679 A comparison of radiation-stress and vortex-force representations. *Journal  
680 of Physical Oceanography* 37, 1122–1141.
- 681 Langmuir, I., 1938. Surface motion of water induced by wind. *Science* 87,  
682 119–123.
- 683 Le, H.A., Lambrechts, J., Ortaleb, S., Gratiot, N., Deleersnijder, E., Soares-  
684 Frazão, S., 2020. An implicit wetting–drying algorithm for the discontinuous  
685 galerkin method: application to the tonle sap, mekong river basin. *Environmental  
686 Fluid Mechanics* , 1–29.
- 687 Le Hénaff, M., Kourafalou, V.H., Paris, C.B., Helgers, J., Aman, Z.M., Hogan,  
688 P.J., Srinivasan, A., 2012. Surface evolution of the Deepwater Horizon  
689 oil spill patch: Combined effects of circulation and wind-induced drift.  
690 *Environmental Science & Technology* 46, 7267–7273.
- 691 Lee, T.N., Leaman, K., Williams, E., Berger, T., Atkinson, L., 1995. Florida  
692 Current meanders and gyre formation in the southern Straits of Florida.  
693 *Journal of Geophysical Research: Oceans* 100, 8607–8620.
- 694 Lee, T.N., Mayer, D.A., 1977. Low-frequency current variability and spin-off  
695 eddies along the shelf off southeast Florida. *Collected Reprints* 1, 344.
- 696 Lee, T.N., Smith, N., 2002. Volume transport variability through the Florida  
697 Keys tidal channels. *Continental Shelf Research* 22, 1361–1377.

- 698 Lee, T.N., Williams, E., 1988. Wind-forced transport fluctuations of the  
699 Florida Current. *Journal of Physical Oceanography* 18, 937–946.
- 700 Li, Z., Johns, B., 1998. A three-dimensional numerical model of surface  
701 waves in the surf zone and longshore current generation over a plane beach.  
702 *Estuarine, Coastal and Shelf Science* 47, 395–413.
- 703 Lin, N., Chavas, D., 2012. On hurricane parametric wind and applications in  
704 storm surge modeling. *Journal of Geophysical Research: Atmospheres* 117.
- 705 Liu, Y., Weisberg, R.H., 2012. Seasonal variability on the West Florida shelf.  
706 *Progress in Oceanography* 104, 80–98.
- 707 Liu, Y., Weisberg, R.H., Zheng, L., 2020. Impacts of hurricane Irma on the  
708 circulation and transport in Florida Bay and the Charlotte Harbor estuary.  
709 *Estuaries and Coasts* 43, 1194–1216.
- 710 Liubartseva, S., Coppini, G., Lecci, R., Clementi, E., 2018. Tracking plastics  
711 in the Mediterranean: 2D Lagrangian model. *Marine Pollution Bulletin*  
712 129, 151–162.
- 713 Longuet-Higgins, M.S., 1970. Longshore currents generated by obliquely  
714 incident sea waves. *Journal of Geophysical Research* 75, 6778–6789.
- 715 Longuet-Higgins, M.S., Stewart, R., 1964. Radiation stresses in water waves;  
716 a physical discussion, with applications, in: *Deep Sea Research and Oceanographic Abstracts*, Elsevier. pp. 529–562.
- 718 Lowe, R.J., Falter, J.L., Bandet, M.D., Pawlak, G., Atkinson, M.J., Moni-  
719 smith, S.G., Koseff, J.R., 2005. Spectral wave dissipation over a barrier  
720 reef. *Journal of Geophysical Research: Oceans* 110.
- 721 Madsen, O.S., Poon, Y.K., Gruber, H.C., 1989. Spectral wave attenuation by  
722 bottom friction: Theory, in: *Coastal Engineering 1988*, pp. 492–504.

- 723 Malmstadt, J., Scheitlin, K., Elsner, J., 2009. Florida hurricanes and damage  
724 costs. *Southeastern Geographer* 49, 108–131.
- 725 McWilliams, J.C., Restrepo, J.M., Lane, E.M., 2004. An asymptotic theory  
726 for the interaction of waves and currents in coastal waters. *Journal of Fluid*  
727 *Mechanics* 511, 135.
- 728 McWilliams, J.C., Sullivan, P.P., 2000. Vertical mixing by Langmuir circula-  
729 tions. *Spill Science & Technology Bulletin* 6, 225–237.
- 730 Mei, C.C., 1989. The applied dynamics of ocean surface waves. volume 1.  
731 World scientific.
- 732 Moon, I.J., Ginis, I., Hara, T., Thomas, B., 2007. A physics-based parame-  
733 terization of air-sea momentum flux at high wind speeds and its impact on  
734 hurricane intensity predictions. *Monthly Weather Review* 135, 2869–2878.
- 735 Pinelli, J.P., Roueche, D., Kijewski-Correa, T., Plaz, F., Prevatt, D., Zisis,  
736 I., Elawady, A., Haan, F., Pei, S., Gurley, K., et al., 2018. Overview of  
737 damage observed in regional construction during the passage of Hurricane  
738 Irma over the State of Florida, in: *Forensic Engineering 2018: Forging*  
739 *Forensic Frontiers*. American Society of Civil Engineers Reston, VA, pp.  
740 1028–1038.
- 741 Powell, M.D., Houston, S.H., Amat, L.R., Morisseau-Leroy, N., 1998. The  
742 HRD real-time hurricane wind analysis system. *Journal of Wind Engineering*  
743 and Industrial Aerodynamics 77, 53–64.
- 744 Powell, M.D., Vickery, P.J., Reinhold, T.A., 2003. Reduced drag coefficient  
745 for high wind speeds in tropical cyclones. *Nature* 422, 279–283.
- 746 Röhrs, J., Christensen, K.H., Hole, L.R., Broström, G., Drivdal, M., Sundby,  
747 S., 2012. Observation-based evaluation of surface wave effects on currents  
748 and trajectory forecasts. *Ocean Dynamics* 62, 1519–1533.

- 749 Schott, F.A., Lee, T.N., Zantopp, R., 1988. Variability of structure and  
750 transport of the Florida Current in the period range of days to seasonal.  
751 *Journal of Physical Oceanography* 18, 1209–1230.
- 752 Siadatmousavi, S.M., Jose, F., Stone, G., 2011. Evaluation of two WAM  
753 white capping parameterizations using parallel unstructured SWAN with  
754 application to the Northern Gulf of Mexico, USA. *Applied Ocean Research*  
755 33, 23–30.
- 756 Sikirić, M.D., Roland, A., Janečković, I., Tomazić, I., Kuzmić, M., 2013.  
757 Coupling of the Regional Ocean Modeling System (ROMS) and Wind  
758 Wave Model. *Ocean Modelling* 72, 59–73.
- 759 Smith, N.P., 1982. Response of Florida Atlantic shelf waters to hurricane  
760 David. *Journal of Geophysical Research: Oceans* 87, 2007–2016.
- 761 Spivakovskaya, D., Heemink, A., Milstein, G., Schoenmakers, J., 2005. Sim-  
762 ulation of the transport of particles in coastal waters using forward and  
763 reverse time diffusion. *Advances in water resources* 28, 927–938.
- 764 Stokes, G.G., 1880. On the theory of oscillatory waves. *Transactions of the*  
765 *Cambridge Philosophical Society* .
- 766 Tolman, H.L., et al., 2009. User manual and system documentation of  
767 WAVEWATCH III TM version 3.14. Technical note, MMAB Contribution  
768 276, 220.
- 769 Van Den Bremer, T., Breivik, Ø., 2018. Stokes drift. *Philosophical Trans-*  
770 *actions of the Royal Society A: Mathematical, Physical and Engineering*  
771 *Sciences* 376, 20170104.
- 772 Villas Bôas, A.B., Cornuelle, B.D., Mazloff, M.R., Gille, S.T., Arduin, F.,  
773 2020. Wave-current interactions at meso-and submesoscales: Insights from  
774 idealized numerical simulations. *Journal of Physical Oceanography* 50,  
775 3483–3500.

- 776 Wachnicka, A., Browder, J., Jackson, T., Louda, W., Kelble, C., Abdelrahman,  
777 O., Stabenau, E., Avila, C., 2019. Hurricane Irmas impact on water quality  
778 and phytoplankton communities in Biscayne Bay (Florida, USA). *Estuaries*  
779 and Coasts , 1–18.
- 780 WAMDI Group, 1988. The WAM model – A third generation ocean wave  
781 prediction model. *Journal of Physical Oceanography* 18, 1775–1810.
- 782 Warner, J.C., Armstrong, B., He, R., Zambon, J.B., 2010. Development of a  
783 coupled ocean–atmosphere–wave–sediment transport (COAWST) modeling  
784 system. *Ocean modelling* 35, 230–244.
- 785 Weisberg, R., Liu, Y., Mayer, D., 2009. Mean circulation on the west Florida  
786 continental shelf observed with long-term moorings. *Geophys. Res. Lett*  
787 36, L19610.
- 788 Weisberg, R.H., Zheng, L., 2006. Hurricane storm surge simulations for  
789 Tampa Bay. *Estuaries and Coasts* 29, 899–913.
- 790 Wu, L., Chen, C., Guo, P., Shi, M., Qi, J., Ge, J., 2011. A FVCOM-  
791 based unstructured grid wave, current, sediment transport model, I. Model  
792 description and validation. *Journal of Ocean University of China* 10, 1–8.
- 793 WW3DG, 2019. User Manual and System Documentation of WAVEWATCH  
794 III Version 6.07, the WAVEWATCH III Development Group. Technical Note  
795 316. NOAA/NWS/ NCEP/MMAB url: <https://github.com/NOAA-EMC/WW3/wiki/files/manual.pdf>.
- 797 Xian, S., Feng, K., Lin, N., Marsooli, R., Chavas, D., Chen, J., Hatzikyriakou,  
798 A., 2018. Brief communication: Rapid assessment of damaged residential  
799 buildings in the Florida Keys after Hurricane Irma. *Natural Hazards and*  
800 *Earth System Sciences* 18, 2041–2045.
- 801 Zedler, S., Niiler, P., Stammer, D., Terrill, E., Morzel, J., 2009. Ocean's  
802 response to Hurricane Frances and its implications for drag coefficient

- 803 parameterization at high wind speeds. Journal of Geophysical Research:  
804 Oceans 114.
- 805 Zhang, C., Durgan, S.D., Lagomasino, D., 2019. Modeling risk of mangroves  
806 to tropical cyclones: A case study of Hurricane Irma. Estuarine, Coastal  
807 and Shelf Science 224, 108–116.